AIP | Journal of Applied Physics

Role of oxygen on microstructure and thermoelectric properties of silicon nanocomposites

G. Schierning, R. Theissmann, N. Stein, N. Petermann, A. Becker et al.

Citation: J. Appl. Phys. **110**, 113515 (2011); doi: 10.1063/1.3658021
View online: http://dx.doi.org/10.1063/1.3658021
View Table of Contents: http://jap.aip.org/resource/1/JAPIAU/v110/i11
Published by the American Institute of Physics.

Role of oxygen on microstructure and thermoelectric properties of silicon nanocomposites

G. Schierning,[1,a)] R. Theissmann,[1] N. Stein,[1] N. Petermann,[1] A. Becker,[1] M. Engenhorst,[1] V. Kessler,[1] M. Geller,[2] A. Beckel,[2] H. Wiggers,[1] and R. Schmechel[1]
[1]*Faculty of Engineering and Center for NanoIntegration Duisburg-Essen (CeNIDE), University of Duisburg-Essen, 47057 Duisburg, Germany*
[2]*Department of Physics and Center for NanoIntegration Duisburg-Essen (CeNIDE), University of Duisburg-Essen, 47057 Duisburg, Germany*

(Received 25 June 2011; accepted 28 September 2011; published online 7 December 2011)

Phosphorus-doped silicon nanopowder from a gas phase process was compacted by DC-current sintering in order to obtain thermoelectrically active, nanocrystalline bulk silicon. A density between 95% and 96% compared to the density of single crystalline silicon was achieved, while preserving the nanocrystalline character with an average crystallite size of best 25 nm. As a native surface oxidation of the nanopowder usually occurs during nanopowder handling, a focus of this work is on the role of oxygen on microstructure and transport properties of the nanocomposite. A characterization with transmission electron microscopy (TEM) showed that the original core/shell structure of the nanoparticles was not found within the sintered nanocomposites. Two different types of oxide precipitates could be identified by energy filtered imaging technique. For a detailed analysis, 3-dimensional tomography with reconstruction was done using a needle-shaped sample prepared by focused ion beam (FIB). The 3-dimensional distribution of silicon dioxide precipitates confirmed that the initial core/shell structure breaks down and precipitates are formed. It is further found that residual pores are exclusively located within oxide precipitates. Thermoelectric characterization was done on silicon nanocomposites sintered between 960 °C and 1060 °C with varying oxygen content between room temperature and 950 °C. The higher sintering temperature led to a better electrical activation of the phosphorus dopant. The oxidic precipitates support densification and seem to be able to reduce the thermal conductivity therefore enhancing thermoelectric properties. A peak figure of merit, zT, of 0.5 at 950 °C was measured for a sample sintered at 1060 °C with a mean crystallite size of 46 nm. © *2011 American Institute of Physics*. [doi:10.1063/1.3658021]

I. INTRODUCTION

Thermoelectric materials are used for solid state cooling or conversion of heat flux into electricity and thermoelectricity will increasingly play a role with respect to the development of a sustainable energy solution by harvesting waste heat of combustion processes.[1–3] As a consequence, research in thermoelectric materials has seen an enormous upturn within the last years. A main focus in thermoelectricity is on the development and utilization of materials with respect to availability and sustainability. Due to its availability and its physical properties, silicon-based nanocrystalline materials are of high interest and investigated increasingly.[4] Nanocrystalline silicon offers a set of principal advantages for thermoelectric applications, motivating the effort of optimizing this material: (i) The raw material is cheap compared to other materials used in thermoelectric generators and highly available at electronic grade quality; (ii) In contrast to many other thermoelectric material systems, silicon is a non-toxic material, which gives a positive impact on the life-cycle management of a thermoelectric generator; (iii) The thermal stability of silicon makes it a highly suitable material for temperatures of 600 K and above, a temperature range in which most nanostructured thermoelectric materials cannot be operated.

Despite these advantages, silicon is *per se* not a preferable thermoelectric material. As a single crystal, it has a high thermal conductivity of 140 W $K^{-1}m^{-1}$ at room temperature,[5] which in turn affects the thermoelectric conversion efficiency negatively.

For a given set of hot and cold junction temperatures, the thermal-to-electrical energy conversion efficiency is directly related to the dimensionless figure of merit zT defined as

$$zT = \frac{\alpha^2 \cdot \sigma}{\kappa} \cdot T, \tag{1}$$

where T is the absolute temperature, α is the Seebeck coefficient, σ is the specific electrical conductivity. $\alpha^2\sigma$ is called power factor, characterizing the material's ability of translating a temperature difference into electrical power, and $\kappa = \kappa_e + \kappa_{ph}$ is the thermal conductivity including the electronic (κ_e) and phonon (κ_{ph}) contribution.

To reduce the lattice thermal conductivity, κ_{ph}, nanostructuring has been shown to effectively scatter phonons in the mid- to long-wavelength regime. Bux *et al.*[4] have

[a)]Author to whom correspondence should be addressed. Electronic mail: gabi.schierning@uni-due.de.

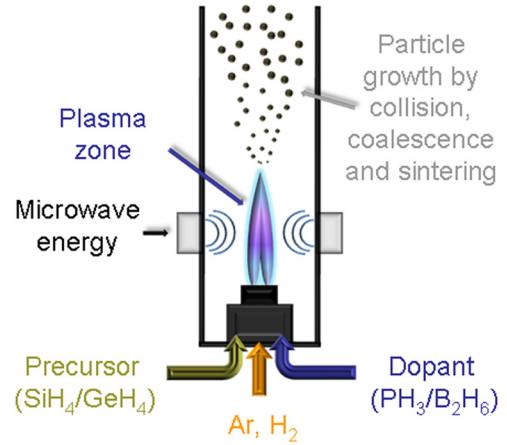

FIG. 1. (Color online) Sketch of the gas phase synthesis for doped silicon nanoparticles. The precursors silane (SiH_4) and phosphine (PH_3) decompose within a microwave induced Ar/H_2 plasma. The shape of the nanoparticles can be tailored by parameters like gas pressure, flow rates, microwave energy, and chemical composition of the gas mixture.

obtained a nanostructured material by a top down-approach, starting with bulk silicon, milling it down to a grain size in the nanometer range, and compacting it again either by hot-pressing or by DC current-assisted sintering technique. The current-assisted sintering approach has been successfully applied for traditional thermoelectric compounds[6] as well as for silicon[4,7] and will be applied in our experiments, too.

In this study, we use a bottom-up approach for the formation of nanostructured silicon based on a direct synthesis of nanomaterials via a gas phase process,[8] sketched in Figure 1. While the milling process has some drawbacks such as the potential risk for unwanted incorporation of impurities and a limit concerning the lowest achievable particle size, gas phase synthesis is a very economic way towards a nanocrystalline material since the intermediate step of producing and milling a bulk material can be avoided. Most importantly, the big advantages of gas phase synthesis are the possibilities for homogeneous doping within a very broad range during particle synthesis and for tuning the crystallite sizes of the sample between a few nm and a few hundred nm.[9] It thus opens the way for a direct synthesis of materials with an optimized composition and size with respect to their thermoelectric properties. An upscaling of the applied gas phase synthesis for industrial processes has already been demonstrated, with nanopowder output in the kg per days range.[10]

Using silicon nanoparticles from such a bottom-up approach via gas phase synthesis implies two possible difficulties. These are the contamination of a material with a high surface-to-volume ratio, especially with oxygen, and the incorporation and electrical activation of the dopant atoms. Considering the whole process chain from precursor decomposition to sintered samples, it is technologically highly demanding to exclude any contamination of the nanopowder with oxygen and moisture. As a result, a Si/SiO_2 core/shell structure is always observed for nanocrystalline silicon powders having been in contact with air. This core/shell structure might considerably hinder the electrical transport and corrupt the thermoelectric properties. Therefore, the goal of this work is to investigate the role of oxygen on microstructure and thermoelectric properties of sintered silicon nanocomposites.

Silicon nanoparticles from the gas phase are usually prepared by temperature- or plasma-induced decomposition of silane.[11–16] The phosphorus incorporation into silicon nanocrystals by adding phosphine to the gas mixture has been addressed by different groups and it has been shown that it is possible to incorporate 100% of the offered P-dopant into the nanocrystals. Nevertheless, most of the phosphorus segregates at the particle surface.[17,18] As a result, Stegner *et al.* found that only around 5% of the incorporated phosphorus was electrically activated[17] and it has been reported that phosphorus located at the surface is bound within the native oxide shell after surface oxidation.[18]

In this paper, we study the role of incorporated oxide in silicon nanocomposites and the interplay between this oxide and the activation of the phosphorus dopant. The paper is organized as follows: In the first part, we will give evidence that the original core/shell structure of silicon/silicon dioxide nanocrystals rearranges during the DC-current sintering. Two different types of oxide precipitates are identified. Possible mechanisms of formation will be discussed. In the second part, we will show and discuss measurements concerning the thermoelectric transport properties of different samples. They vary with respect to the original oxygen content and the sintering temperature. Both are crucial factors for the thermoelectric performance of the material, as it will be shown that they influence the electrically activated dopant concentration.

II. EXPERIMENTAL

A. Sample preparation

Silicon nanoparticles were synthesized in a gas phase process based on the decomposition of silane (SiH_4) in a microwave plasma reactor as described elsewhere.[8,19] The variation of microwave power, pressure, and precursor concentration enables for the formation of crystalline particles with different mean particle diameter. N-type doping was realized by adding 1% of phosphine (PH_3) to the precursor gas leading to a nominal dopant concentration of $5 \times 10^{20}\,cm^{-3}$ for all samples. Two different batches of silicon nanopowder were synthesized to obtain two materials with differing mean particle diameter.

The batches of the as-prepared nanoparticles were further processed by DC-current sintering, using a SPS machine from *FCT Systeme GmbH*. Several grams of nanoparticles were pre-compacted and subsequently sintered to dense pellets at a pressure of 35 MPa using graphite crucibles and dies. The temperature was measured by a pyrometer at the bottom of the upper graphite die and the heating rate was fixed at 100 K/min. For all samples, the dwell time at the sintering temperature was set to 3 min. The furnace was kept in an argon atmosphere during the whole sintering process. Two samples were prepared from each silicon powder and sintered at 960 °C and 1060 °C, respectively.

B. X-ray diffraction and density

The average isotropic crystallite diameter of the raw powder and the sintered pellets was obtained by x-ray diffraction (XRD) combined with Rietveld-analysis and the density of the sintered pellets was measured by the Archimedes principle. The XRD measurements of the powders were conducted by means of a *Siemens* D5000 diffractometer in transmission geometry using quartz glass capillaries and the data were evaluated by the software package FULLPROF.[20] All samples were refined using the identical set of parameters. The mean particle diameter calculated from these results was 15 nm and 24 nm, respectively. Typical particle size distributions silicon nanopowder analogue to the one used here from this process were shown in Ref. 21. Assuming a similar distribution as in Ref. 21, we can estimate the 1σ confidence interval to be $10\,\text{nm} < D_{1\sigma} < 20\,\text{nm}$ for the smaller batch and $20\,\text{nm} < D_{1\sigma} < 40\,\text{nm}$ for the larger one. The sintered pellets were pestled thoroughly and then measured likewise. All materials have an almost identical lattice constant of $a_0 \approx 5.417$ Å which is explicitly smaller than the lattice constant of bulk single crystalline silicon ($a_0 = 5.429$ Å (Ref. 22)).

Table I summarizes the results obtained from XRD investigations and density measurement of the sintered samples. The density of all samples is around 95% to 96% compared to the density of single crystalline silicon. The smallest crystallite diameter of a sintered pellet was 25 nm, realized by sintering the 15 nm raw powder at 960 °C while the largest crystallite diameter of this series was 46 nm, obtained by sintering the same raw powder at 1060 °C.

C. Microstructural characterization

The nanostructure of the sintered samples was characterized by transmission electron microscopy (TEM) by means of a 200 keV *Philips, Tecnai* F20 ST. All samples were cut into pieces and subsequently grinded down to a thickness of approximately 40 μm. Final thinning to electron transparency was achieved by a precision ion polishing system (*PIPS, Gatan 691*) with Ar ions. As the investigation of the oxide phase is one key interest of this work, energy filtered TEM (EFTEM) imaging technique was used to visualize the contrast between silicon and silicon dioxide. For this, the energy filter was set either at 17 eV or at 24 eV, making use of the plasmon energy of silicon and silicon dioxide, respectively. For a 3-dimensional tomography of the sintered material, one needle-shaped sample was prepared from pellet C (Table I) using a focused ion beam (FEI *Nanolab*). The images for electron tomography were acquired in the scanning transmission electron microscopy (STEM) mode, in order to suppress diffraction contrast. The observed Z-contrast was interpreted based on results obtained from the EFTEM and bright-field imaging. The tilt series was acquired using a linear tilt scheme with 1° increments for angles between −75° and 75° with a *Fishione* tomography holder. Data reconstruction was done with the software package INSPEC3D, visualization with the software package AMIRA.

TABLE I. Comparison of structure data of silicon nanocomposites. Mean isotropic crystallite diameter was obtained by XRD measurement and Rietveld refinement. Density in percentage of single crystalline silicon was measured by Archimedes method. Density of single crystalline silicon is 2.33 g/cm^3.

	Identification	T_{sinter}	Mean diameter	Density
Diameter of the raw powder: ~24 nm	Pellet *A*	960 °C	37 nm	95.1%
	Pellet *B*	1060 °C	44 nm	95.8%
Diameter of the raw powder: ~15 nm	Pellet *C*	960 °C	25 nm	94.8%
	Pellet *D*	1060 °C	46 nm	95.7%

D. Thermoelectric transport properties

The Seebeck coefficient α and the electrical conductivity σ were measured by a direct measuring technique using the commercial system ZEM-3 from *Ulvac Technologies, Inc.* The charge carrier concentration and mobility of all samples were estimated from the thermoelectric transport properties. Highly doped silicon samples as used in our experiments can be considered as degenerated semiconductors. Then, α is a function of the charge carrier concentration n and the effective mass of the charge carriers m^*

$$\alpha = \frac{8 \cdot \pi^2 \cdot k_b^2}{3 \cdot e \cdot h^2} \cdot m^* \cdot T \cdot \left(\frac{\pi}{3 \cdot n}\right)^{2/3}, \tag{2}$$

where k_b is the Boltzmann constant, h is Planck's constant, and e is the charge of the electron.[1] This transport model has been derived from Boltzmann transport theory, using a single parabolic band and energy independent scattering approximation.[23] Equation (2) represents the situation in a thermoelectric material quite decently. The charge carrier concentration of all samples was calculated according to Eq. (2) from the derivative $\left|\frac{\partial \alpha}{\partial T}\right|$ in the linear regime (RT to 700 °C), using $m_e^* = 1.13\, m_{e,0}$ (Ref. 24) as effective mass of the electrons. The mobility of the charge carriers, μ, was calculated from the specific electrical conductivity σ according to

$$\sigma = n \cdot e \cdot \mu, \tag{3}$$

using the charge carrier concentration n obtained from the Seebeck-measurement.

For comparison, a single sample (sample C) was also characterized by a Hall measurement using the van-der-Pauw method for sample structures with arbitrary shape.[25] The sample was thinned (having a thickness of 200 μm determined by scanning electron microscopy) and cut into a rectangle shape with contacts in all four corners. The Hall measurement was performed in a bath cryostat with a superconducting magnet for a magnetic field of B = 10 T.

A laser flash method LFA 457 MicroFlash from *NETZSCH Gerätebau GmbH* was used for the characterization of the thermal diffusivity of the sintered samples. The heat capacity was measured using differential scanning calorimetry, DSC 404, from *NETZSCH Gerätebau GmbH*.

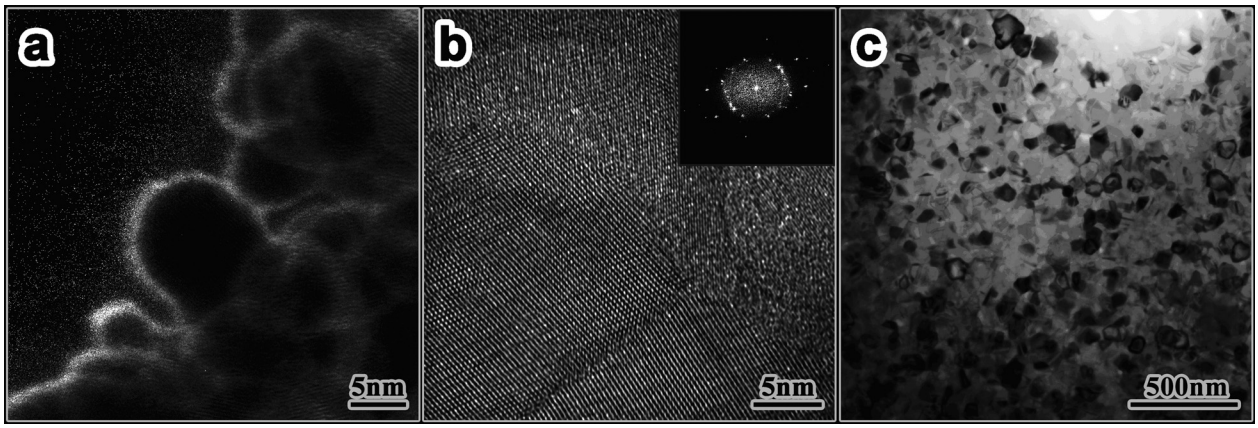

FIG. 2. (a) Core/shell structure of silicon raw powder: Energy filtered ratio image enhances the contrast of the SiO_2-edge around the Si particle. The Si-rich areas appear dark and the SiO_2-rich areas appear bright. (b) High resolution TEM image of a sintered pellet (pellet C). Typically, no evidence is found for an oxide shell after sintering. (c) Typical bright field image of a sintered pellet (pellet B) showing the nanocrystalline microstructure.

III. RESULTS AND DISCUSSION

A. Evidence for silicon dioxide precipitates

The morphology, structure, and chemical composition of the raw powder and the sintered silicon samples (Pellets A-D, see Table I) were characterized by transmission electron microscopy. Energy filtered (EF-TEM) imaging was used to observe the contrast between silicon and silicon dioxide. Figure 2(a) shows the core/shell structure typically found for silicon nanoparticles which were exposed to ambient conditions. An oxide layer with a thickness of around 0.5 to 1 nm covers the silicon core. After sintering (Figure 2(b)), no evidence is found for an oxide layer at grain boundaries between adjacent grains, but an overall nanocrystalline structure is obtained (Figure 2(c)).

A typical energy filtered image of a sintered pellet is shown in Figure 3. Assuming a mean thickness of 0.5 nm for the native oxide covering the surface of the as-prepared silicon nanoparticles results in a SiO_2 mass fraction of 10% and 6% for the 15 nm and 24 nm particles, respectively. From Figure 3, it can be seen that the original core/shell structure of the as-prepared particles was not preserved after sintering. Instead, the silicon dioxide has rearranged and segregated in separate precipitates. Two types of oxide phase regions, differing in size and shape, can be found, marked with 1 and 2 in Figures 3(b) and 3(c). We attribute the bigger precipitates of type 1 to a viscous flow sintering driven by surface forces, as it is the well-known sintering process for silica.[26,27] When the DC-current sintering starts, the thin native oxide layer is assumed to electrically break down as found for other current-sintered materials[28,29] and due to the dissipation of electrical energy the system is heated. At elevated temperatures, the viscosity of the amorphous oxide is sufficiently low to enable a fast sintering process based on the viscous flow of silica.

Type 2 precipitates are well known from Czochralski silicon and appear due to the fact that silicon has a higher solubility for oxygen close to the melting temperature compared to room temperature. As a result, upon cooling the solubility of oxygen drops and the oxide precipitates.[30] Whereas type 1 precipitates seem to be located preferably at triple points between different silicon grains, type 2 precipitates are mostly found in the middle of silicon grains. We attribute the fact that the two types differ slightly in

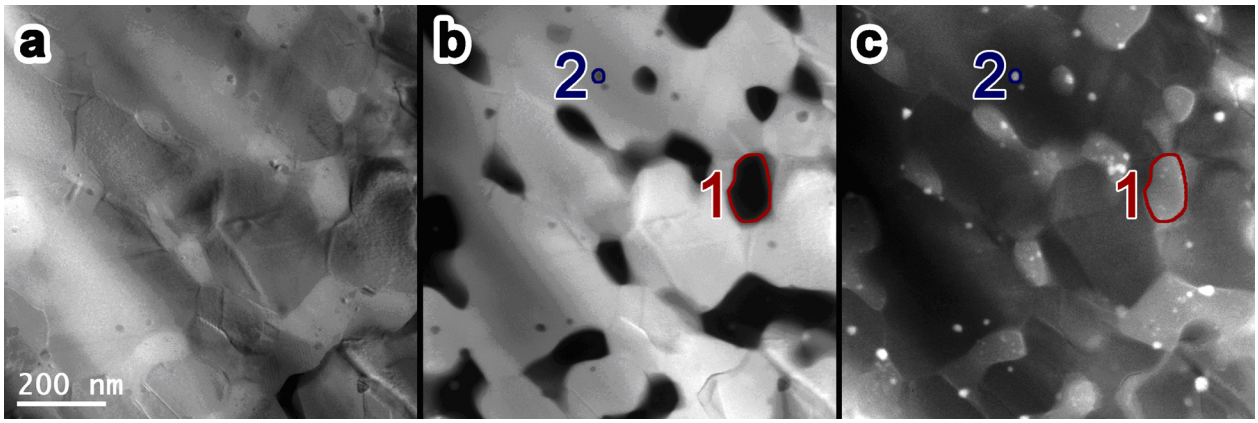

FIG. 3. (Color online) Energy filtered TEM of a nanocrystalline silicon, sintered at 1060 °C. (a) Bright field contrast showing a densely sintered sample. The filter was set at 17 eV (b) and 24 eV (c) making use of the plasmon energy of silicon and silicon dioxide, respectively. In (b) silicon appears bright and silicon dioxide appears dark. Inversed contrast is given in (c). Two different types of silicon dioxide precipitates can be identified marked with 1 and 2 in (b) and (c), originating from a rearrangement of the initial oxide shell (1) and due to precipitation because of the solubility limit of oxygen in silicon (2).

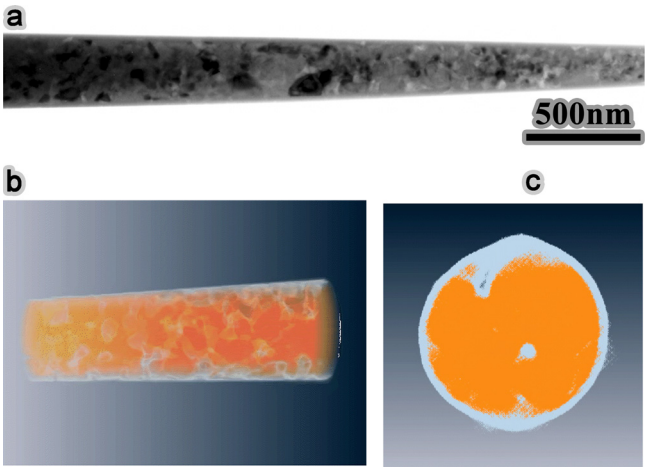

FIG. 4. (Color online) (a) Bright-field image of a cylindrical sample prepared from pellet C by FIB used to obtain a tilt-series for 3-dimensional reconstruction. (b) Reconstructed 3-dimensional image showing the distribution of oxygen rich regions within the silicon matrix. (c) Cross section through the reconstructed image showing a connected silicon matrix with isolated silicon dioxide precipitates. Pores (dark contrast) are located within the silicon dioxide (enhanced online) [URL:http://dx.doi.org/10.1063/1.3658021.1].

contrast (Figure 3(c)) to a different stoichiometry of the segregated oxide. While type 1 precipitates are assumed to be substoichiometric SiO_x with $x < 2$, type 2 precipitates are expected to consist of stoichiometric SiO_2 being released from the surrounding silicon matrix due to disproportionation,[31]

$$SiO_x \rightarrow \frac{x}{2} SiO_2 + \left(1 - \frac{x}{2}\right) Si\,. \tag{4}$$

Characteristic SiO_2 precipitates of type 2 have been found earlier in hot pressed pellets ($T > 900\,^{\circ}C$) made of very similar silicon nanoparticles.[32]

In order to get an impression of the 3-dimensional distribution of silicon and oxidic precipitates, a piece of pellet C was prepared for TEM tomography. For this, a cylinder with very homogeneous diameter of about 350 nm was prepared by focused ion beam to allow for a 3-dimensional reconstruction. Figure 4(a) shows a bright-field TEM image of the needle-shaped sample. As the diameter of the cylinder is thin enough for transmission electron microscopy, the nanocrystalline structure of the sintered pellet can clearly be seen. In Figure 4(b), a screenshot of the 3-dimensional reconstruction is given (movie with rotating cylinder is available online). As also obvious from Fig. 4, a continuous silicon network with embedded precipitates is observed. The reconstructed 3D image of the sample also shows distributed islands of oxide rich regions (type 1) within the silicon matrix, indicating that the core/shell structure of the as-prepared particles has completely vanished.

From Figure 4(c), it becomes clear how the pores which are responsible for incomplete densification are distributed within the sample with respect to the two phases, silicon and silicon oxide. A detailed analysis of all single slices of the reconstruction clearly shows that pores are exclusively located within the oxidic precipitates, while no pores were found within the silicon matrix. From the distribution within the investigated needle, we estimated the content of silicon, silicon oxide, and pores: It is 89 at. % of silicon, 9 at. % of silicon oxide, and 2% of pores. This matches well with the assumption that the mean thickness of the native oxide is about 0.5 nm. The over-all density of the sintered sample, determined by the Archimedes principle, is 95% (see pellet *C* in Table I), indicating 5% of pores. As TEM in general investigates only a small sample-volume, local fluctuations may be the origin of this deviation as well as variations in the density or assumed thickness of SiO_x.

From the microstructural analysis, it can be stated that the DC-sintered pellets are nanocrystalline. The SiO_x-shell supports viscous flow sintering of the nanoparticles leading to oxidic precipitates with a typical dimension of around 100 nm, while the silicon/silicon grain boundaries seem to be oxygen-free. Additionally, very small precipitates of type 2 are formed based on the segregation of silica from oxygen-rich silicon.

B. Thermoelectric properties

In Sec. B, the thermoelectric properties of the sintered silicon nanocomposites will be characterized and discussed especially with respect to the role of the oxidic precipitates. Figure 5 presents the results received from the characterization of the thermoelectric transport properties of 4 sintered pellets, all with nominally identical phosphorus concentration of $5 \times 10^{20}\,cm^{-3}$ (1 at. %). The samples vary in sintering temperature (960 °C and 1060 °C) and in mean diameter of the raw powder used (15 nm and 24 nm). Table I gives a compilation of structural data of all pellets. Because of coarsening effects, the final crystallite sizes of the 1060 °C-sintered samples (raw powders: 15 nm and 24 nm) are very similar, i.e., 44 nm and 46 nm. Therefore, it can be stated that these two samples mostly differ with respect to oxygen content. The sample with smaller initial particles contains considerably more oxygen than the sample with larger initial diameter due to its significantly higher surface-to-volume ratio.

With respect to the electric transport properties, the sintering temperature seems to be more important than the initial particle size, which is related to the oxygen content (Fig. 5). The Seebeck coefficients of all samples is negative, indicating n-type transport, and its absolute value increases up to temperatures of around 700 °C, which is a typical behaviour for metals and degenerated semiconductors. The electrical conductivity of the 1060 °C sintered samples is higher than for the 960 °C sintered samples and a metallic temperature characteristic, in the sense of a decreasing conductivity with increasing temperature, is observed. In contrast, the 960 °C sintered samples hardly show any temperature dependence of the electrical conductivity in the observed temperature range.

In order to get deeper insight into the electric transport mechanism, the charge carrier density and mobility of all samples were estimated from the thermoelectric transport properties as described above. The results are given in Table II. The charge carrier concentration of all samples is around 2.1 to $2.2 \times 10^{20}\,cm^{-3}$, obviously independent from

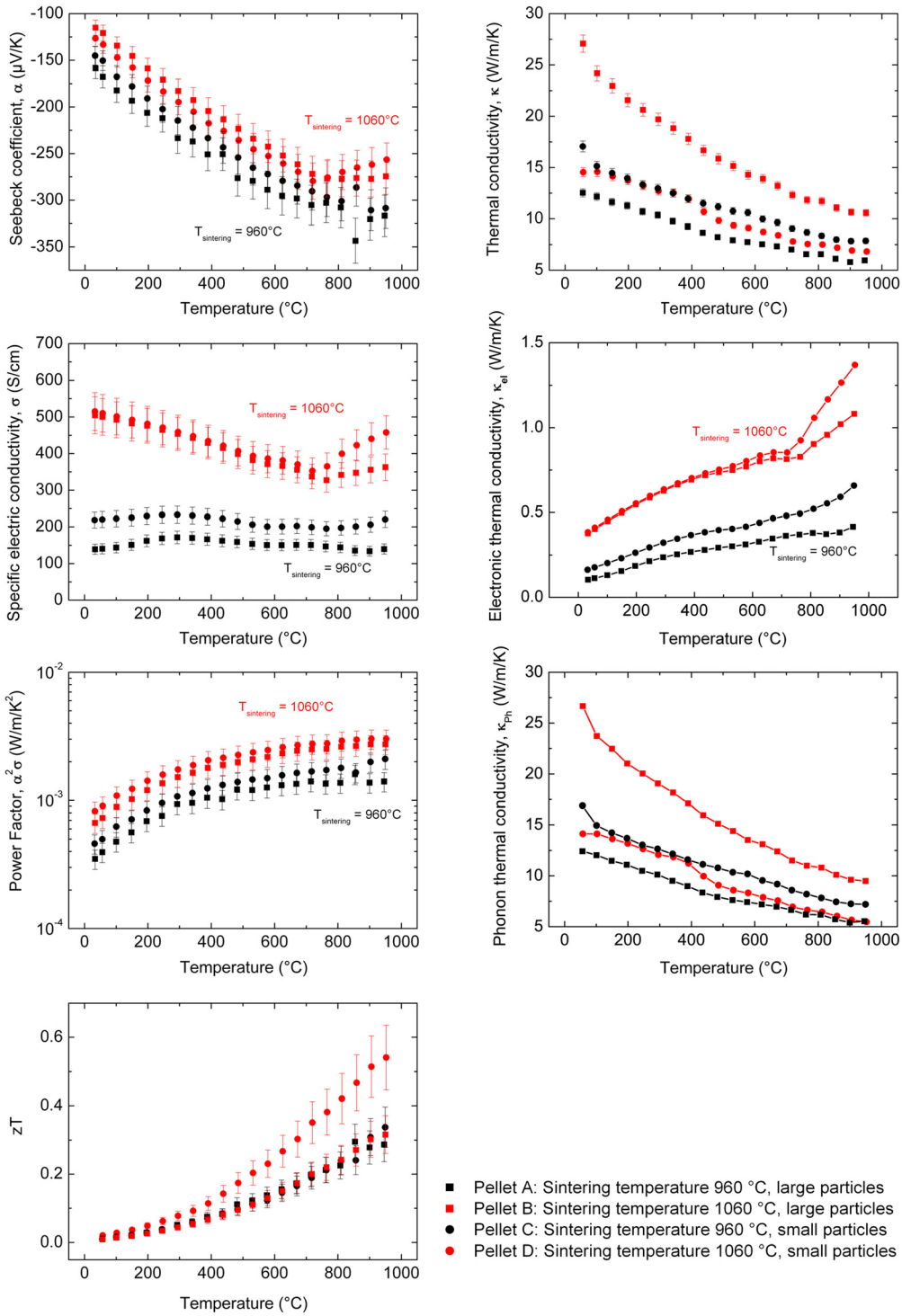

FIG. 5. (Color online) Thermoelectric characterization of 4 nanocrystalline n-type doped silicon samples details of which are given in Table I. The samples vary in sintering temperature (black: 960 °C and red: 1060 °C) and in the mean diameter of the raw powder (circle: 15 nm and square: 24 nm). Seebeck coefficient α and electrical conductivity σ are measured using a direct measurement technique, the power factor $\alpha^2\sigma$ is calculated from α and σ, respectively. Thermal conductivity is measured using a Laser-Flash method. Electronic thermal conductivity is calculated using the Wiedemann-Franz-Law ($L = 2.44 \times 10^{-8}$ W Ω /K^2), phonon thermal conductivity from $\kappa = \kappa_{el} + \kappa_{ph}$. Figure of merit is calculated from the single measurements. A peak zT of 0.5 at 950 °C was obtained for pellet D.

the sintering temperature and initial particle size. The differences in electrical conductivity are therefore mainly the result of different charge carrier mobilities. For the samples sintered at 960 °C, the analysis yields a charge carrier mobility of 4 resp. 6 $cm^2V^{-1}s^{-1}$, while for the samples sintered at 1060 °C, a mobility of 15 $cm^2V^{-1}s^{-1}$ is obtained, each calculated from the room temperature values of the specific electrical conductivity. This difference in mobility directly translates into higher zT values if the low thermal conductivity may be preserved (sample D). Note that a mobility of 15 $cm^2V^{-1}s^{-1}$ is very close to the mobility of the optimized samples from Bux *et al.*,[4] so that the main

TABLE II. Charge carrier concentration and mobility. Charge carrier concentration calculated from the derivative of the Seebeck-coefficient with respect to temperature in the linear regime (RT to 700 °C). Mobility calculated from the specific electrical conductivity at room temperature, according to the Drude model.

	Identification	T_{sinter}	$\left\|\frac{\partial\alpha}{\partial T}\right\|$ (μV/K^2)	σ (T = 300 K) (S/cm)	n; from $\left\|\frac{\partial\alpha}{\partial T}\right\|$ (10^{20} cm^{-3})	μ (cm^2/V/s)
Diameter of the raw powder: ~24 nm	Pellet *A*	960 °C	$2.0911 \cdot 10^{-7}$	140	2.2	4
	Pellet *B*	1060 °C	$2.1741 \cdot 10^{-7}$	505	2.1	15
Diameter of the raw powder: ~15 nm	Pellet *C*	960 °C	$2.0549 \cdot 10^{-7}$	220	2.2	6
	Pellet *D*	1060 °C	$2.0877 \cdot 10^{-7}$	515	2.2	15

difference between nanocrystalline silicon from a ball milling process and from the bottom-up approach, presented here, seems to be the lower charge carrier concentration. The charge carrier concentrations of our samples, estimated from the thermoelectric transport measurements, are significantly lower than the nominal doping concentration of 5×10^{20} cm^{-3}. This difference between observed and nominal concentration is most probably caused by the fact that most of the phosphorus dopants are located close to the surface of the initial particles and are therefore within the oxide.[17] The solubility of phosphorus in silicon is 2.4 at. % at 1180 °C (Ref. 33) and the P-Si binding is generally preferred compared to the P-O binding. Therefore, diffusion of the phosphorus from the Si/SiO_x interface into the silicon matrix would be expected. Due to the nanocrystalline nature of the material, the necessary diffusion paths are short. Nevertheless, temperatures of at least 900 °C are required,[34] and it is found that P diffuses 0.6 nm in SiO_2 at 900 °C within 1 h while it diffuses approximately 20 nm in Si under same conditions.[35] As a result, the release of phosphorus from the oxide is considered as the limiting process for charge carrier concentration enhancement.

The samples sintered at 1060 °C show an increase in electrical conductivity as well as a decrease of the absolute value of the Seebeck-coefficient above 720 °C (Fig. 5). In principal, such behaviour could be the result of the thermal generation of intrinsic charge carriers. However, the intrinsic carrier concentration in silicon at 1000 °C is in the order of 10^{18} cm^{-3} (Ref. 36), which is about two orders of magnitude less than the estimated extrinsic carrier concentration. Thus, intrinsic carrier effects can be neglected, and consequently, this behaviour has to be attributed to an increase of extrinsic charge carrier concentration. A release of additional dopants from oxide precipitates during the measurement is unlikely with respect to the very low diffusivity of phosphorus in SiO_2, as discussed above. The increase of extrinsic charge carriers above 720 °C is therefore attributed to an "activation" of additional dopants according to the solubility limit of phosphorus in silicon.[33] This is demonstrated by the model shown in Figure 6. The charge carrier density can be assumed to be constant below 720 °C (depletion of dopants), in accordance with a linear decrease of the Seebeck-coefficient, exemplarily shown for sample D (Fig. 6). Above this temperature, the charge carrier concentration raises because the solubility limit of phosphorus increases. This translates into a decrease of the absolute value of the Seebeck-coefficient. It is a typical behaviour for highly phosphorus doped nanosilicon samples and has been observed in Ref. 4, too.

In contrast to the samples sintered at 1060 °C, the samples sintered at 960 °C show no significant change in electrical conductivity over the whole measured temperature range. The analysis of the Seebeck coefficient yields the same temperature-independent charge carrier concentration for temperatures up to 720 °C. Consequently, the charge carrier mobility in these samples is mainly temperature independent. Such a temperature independent mobility could be an indication for an intermediary transport process between band-like transport in extended states and hopping transport in localized states. A band-like transport in extended states yields a decreasing mobility with increasing temperature due to scattering with phonons. In contrast, hopping transport between localized states requires phonons and, therefore, the mobility increases with temperature. Band-like transport in extended states is usually related to mobilities above 10 cm^{2}V^{-1}s^{-1}.[37] The samples sintered at 1060 °C fulfil this requirements and the mobility decreases with temperature as expected for transport in extended states. In contrast, hopping transport between localized states yields mobilities below 1 cm^2 V^{-1}s^{-1}.[37] The mobility range between 1 and 10 cm^{2}V^{-1}s^{-1} is an intermediary range, where temperature independent mobilities are observed quite often, for example, also for

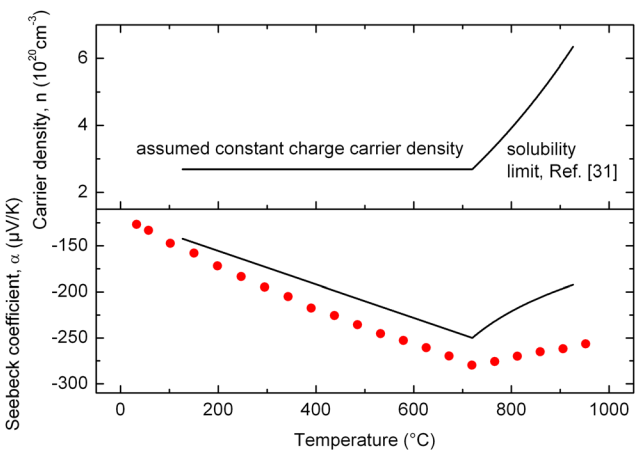

FIG. 6. (Color online) Model of the charge carrier density and Seebeck-coefficient as a function of the solubility limit of phosphorus in silicon.[33] Below 720 °C, the charge carrier density is assumed to be constant because of depletion of impurities. Above, the solubility limit of phosphorus rises and more dopant atoms become activated. The consequence is a kink in the Seebeck coefficient, exemplarily shown for sample D, as well as an increase of the specific electrical conductivity.

organic crystals.[38] The samples sintered at 960 °C exhibit charge carrier mobilities exactly in this intermediary range. Therefore, it can be expected that localized states are much more relevant for charge transport in these samples compared to the samples sintered at 1060 °C. The larger dominance of localized states might cause that the observation of "activated" donors above 720 °C is less pronounced in the samples sintered at 960 °C, because additional "activated" charge carriers may easily get trapped in localized states.

Since the analysis of charge carrier density and mobility from the Seebeck-coefficient is less common, the charge carrier concentration and mobility has exemplarily been estimated by a Hall measurement for sample C. This measurement yields a charge carrier concentration of $n = 3 \times 10^{20}\,cm^{-3}$ and a mobility of $\mu = 5\ cm^2V^{-1}s^{-1}$ at $T = 300\,K$, determined under a magnetic field of $B = 10\,T$. Hence, the results for the charge carrier concentration and mobility from the Hall measurement are in good agreement with the Seebeck measurement, even though the Hall effect is quite sensitive to the local geometry/topology of the transport states.[39–41]

Concerning the thermal transport properties, the initial particle size, which was related to the oxygen content, has more influence (Fig. 5). Especially, for the samples sintered at 1060 °C, a significant difference in the thermal conductivity appears, while the electrical conductivity is almost equal. The highest thermal conductivity is observed for large grain sizes and low oxide content. For low sintering temperatures, the quality of the grain boundaries becomes more dominant.

A high thermoelectric efficiency requires both good electric transport and low thermal shunt. The sample made from the nanopowder with larger mean diameter and sintered at 1060 °C (pellet B) showed the highest thermal conductivity of $27\,W\,K^{-1}m^{-1}$ at room temperature of all samples investigated. The lowest thermal conductivity achieved was around $6\,W\,K^{-1}m^{-1}$ at 900 °C, measured in pellet A. Single crystalline silicon has a thermal conductivity approximately around $140\,W\,K^{-1}m^{-1}$ at room temperature[5] which is one order of magnitude higher than the measured data of the nanocrystalline silicon.

The resulting figure of merit is best for pellet D (small mean diameter of the starting powder, high sintering temperature), with a peak zT of 0.5 at 950 °C. Pellet D has a mean crystallite diameter of 46 nm and best performance of the power factor at reasonably small values for the thermal conductivity.

IV. CONCLUSION

Nanocrystalline bulk silicon was fabricated from silicon nanoparticles applying a synthesis from the gas phase and subsequent DC-current sintering. The nanocrystalline character of the sintered samples was demonstrated by transmission electron microscopy. Using a cylinder prepared by focused ion beam, a 3-dimensional tomography was carried out. Reconstructed data show oxide precipitates homogeneously distributed within the sample. Two different types of oxide precipitates have been identified and their origin discussed. Other than in the Si-core/SiO_2-shell structure of the starting nanopowder, the sintered nanocomposites perfectly allow for electrical percolation within the silicon matrix. With higher sintering temperature, the charger carrier mobility is higher due to a better crystalline quality of the samples. The determined charge carrier concentration is significantly below the nominal doping concentration, because a considerable percentage of the dopant atoms is bound within the oxidic precipitate. Therefore, the diffusion of the phosphorus dopant from the oxidic phase onto substitutional lattice sites of the silicon is a crucial issue. Our results suggest that at least a minimum concentration of oxygen might be favourable for the formation of silicon-based thermoelectrics to enhance densification and to lower thermal conductivity while the sintering parameters also have to be optimized with respect to dopant diffusion into the silicon lattice.

ACKNOWLEDGMENTS

We thank M. Farle and A. Lorke, both department of experimental physics, for the possibility to use the microscopy facilities, and J. Gündel-Graber, department of inorganic chemistry, for the XRD measurements. Financial support by the Deutsche Forschungsgemeinschaft within the priority program on nanoscaled thermoelectricity, SPP 1386, and by the European Union and the Ministry of Innovation, Science and Research of the State of North Rhine-Westphalia, Germany, in the framework of an Objective 2 Programme (European Regional Development Fund, ERDF) and a Young Researcher Grant is gratefully acknowledged.

[1] G. J. Snyder and E. S. Toberer, Nature Mater. **7**(2), 105 (2008).
[2] M. S. Dresselhaus, G. Chen, Z. F. Ren, G. Dresselhaus, A. Henry, and J.-P. Fleurial, JOM **61**(4), 86 (2009).
[3] A. Eder and J. Liebl, "Thermoelectric waste heat recovery: A technology transfer from aerospace to the automotive industry?," in *Thermoelektrik—Eine Chance für die Automobilindustri*e, edited by D. Jänsch (Expertverlag, Renningen, Germany, 2008), p. 45.
[4] S. K. Bux, R. G. Blair, P. K. Gogna, H. Lee, G. Chen, M. S. Dresselhaus, R. B. Kaner, and J.-P. Fleurial, Adv. Mater. **19**(15), 2445 (2009).
[5] D. G. Cahill, W. K. Ford, K. E. Goodson, G. D. Mahan, A. Majumdar, H. J. Maris, R. Merlin, and S. R. Phillpot, J. Appl. Phys. **93**(2), 793 (2003).
[6] B. Poudel, Q. Hao, Y. Ma, Y. Lan, A. Minnich, B. Yu, X. Yan, D. Wang, A. Muto, D. Vashaee, X. Chen, J. Liu, M. S. Dresselhaus, G. Chen, and Z. Ren, Science **320**, 634 (2008).
[7] D. Schwesig, G. Schierning, R. Theissmann, N. Stein, N. Petermann, H. Wiggers, and R. Schmechel, Nanotechnology **22**, 135601 (2011).
[8] N. Petermann, N. Stein, G. Schierning, R. Theissmann, B. Stoib, C. Hecht, C. Schulz, and H. Wiggers, J. Phys. D **44**, 174034 (2011).
[9] U. Kortshagen, J. Phys. D **42**, 113001 (2009).
[10] T. Hülser, S. M. Schnurre, H. Wiggers, and C. Schulz, KONA-Powder and Particle J., No. **29** (2011).
[11] N. Rao, S. Girshick, J. Heberlein, P. McMurry, S. Jones, D. Hansen, and B. Micheel, Plasma Chem. Plasma Process. **15**(4), 581 (1995).
[12] M. Otobe, T. Kanai, T. Ifuku, H. Yajima, and S. Oda, J. Non-Cryst. Solids **198–200**(2), 875 (1996).
[13] H. Wiggers, R. Starke, and P. Roth, Chem. Eng. Technol. **24**, 261 (2001).
[14] M. T. Swihart, Curr. Opin. Colloid Interface Sci. **8**, 127 (2003).
[15] A. Bapat, C. Anderson, C. R. Perrey, C. B. Carter, S. A. Campbell, and U. Kortshagen, Plasma Phys. Controlled Fusion **46**(12B), B97 (2004).
[16] L. Mangolini, E. Thimsen, and U. Kortshagen, Nano Lett. **5**, 655 (2005).
[17] A. R. Stegner, R. N. Pereira, R. Lechner, K. Klein, H. Wiggers, M. Stutzmann, and M. S. Brandt, Phys. Rev. B **80**(16), 165326 (2009).
[18] X. D. Pi, R. Gresback, R. W. Liptak, S. A. Campbell, and U. Kortshagen, Appl. Phys. Lett. **92**, 123102 (2008).
[19] J. Knipping, H. Wiggers, B. Rellinghaus, P. Roth, D. Konjhodzic, and C. Meier, J. Nanosci. Nanotechnol. **4**(8), 1039 (2004).

[20]J. Rodriguez-Carvajal. "FULLPROF: A program for rietveld refinement and pattern matching analysis," in *Abstracts of the Satellite Meeting on Powder Diffraction of the XV Congress of the IUCr* (Toulouse, France, 1990), p. 127.
[21]G. Schierning, T. Claudio, R. Theissmann, N. Stein, N. Petermann, A. Becker, J. Denker, H. Wiggers, R. P. Hermann, and R. Schmechel, Mater. Res. Soc. Symp. Proc. **1267**, 1267 (2010).
[22]*CRC Handbook of Chemistry and Physics*, edited by D. R. Lide, 90th ed. 2009–2010 ed. (CRC, Boca Raton, London, New York, 2009).
[23]M. Cutler, J. F. Leavy, and R. L. Fitzpatrick, Phys. Rev. **133**, A1143 (1964).
[24]M. A. Green, J. Appl. Phys. **67**(6), 2944 (1990).
[25]L. J. van der Pauw, Philips Tech. Rev. **20**, 220 (1958).
[26]M. J. Kirchhof, H. J. Schmid, and W. Peukert, Rev. Sci. Instrum. **75**(11), 4833 (2004).
[27]M. J. Kirchhof, H. J. Schmid, and W. Peukert, Phys. Rev. E **80**(2), 026319 (2009).
[28]G. Xie, O. Ohashi, N. Yamaguchi, M. Song, K. Mitsuishi, K. Furuya, and T. Noda, Japanese J. Appl. Phys. **42**, 4725 (2003).
[29]G. Xie, O. Ohashi, M. Song, K. Furuya, and T. Noda, Metall. Mater. Trans. **34A**, 699 (2003).
[30]G. Kissinger, D. Kot, J. Dabrowski, V. Akhmetov, A. Sattler, and W. Von Ammon, ECS Trans. **16**(6), 97 (2008).
[31]B. J. Hinds, F. Wang, D. M. Wolfe, C. L. Hinkle, and G. Lucovsky, J. Non-Cryst. Solids **227–230**(Part 1), 507 (1998).
[32]G. Schierning, R. Theissmann, H. Wiggers, D. Sudfeld, A. Ebbers, D. Franke, V. T. Witusiewicz, and M. Apel, J. Appl. Phys. **103**(8), 084305 (2008).
[33]R. W. Olesinski, N. Kanani, and G. J. Abbaschian, Bull. Alloy Phase Diagrams **6**(2), 130 (1985).
[34]M. Perego, C. Bonafos, and M. Fanciulli, Nanotechnology **21**(2), 025602 (2010).
[35]S. M. Sze, *Semiconductor Devices: Physics and Technology*, 2nd ed. (Wiley, New York, 2001).
[36]S. M. Sze and K. K. Ng, *Physics of Semiconductor Devices*, 3rd ed. (Wiley Interscience, John Wiley & Sons, Inc., Hoboken, NJ, 2007).
[37]N. F. Mott and E. A. Davis, *Electronic Processes in Non-crystalline Materials* (Oxford University Press, New York, 1979).
[38]I. N. Hulea, S. Fratini, H. Xie, C. L. Mulder, N. N. Iossad, G. Rastelli, S. Ciuchi, and A. F. Morpurgo, Nature Mater. **5**, 982 (2006).
[39]D. Emin, Philos. Mag. **35**, 1189 (1977).
[40]M. Y. Kharitonov and K. B. Efetov, Phys. Rev. B **77**, 045116 (2008).
[41]A. Gondorf, M. Geller, J. Weißbon, and A. Lorke, Phys. Rev. B **83**, 212201 (2011).